PHYSICAL REVIEW B **108**, 085432 (2023)

Symmetry-driven persistent spin texture for the two-dimensional nonsymmorphic CdTe and ZnTe crystal structures

Manish Kumar Mohanta [*] and Puru Jena [†]
Department of Physics, Virginia Commonwealth University, Richmond, Virginia 23284, USA

(Received 11 April 2023; revised 10 July 2023; accepted 4 August 2023; published 29 August 2023)

In this paper, two nonsymmorphic two-dimensional structures of CdTe and ZnTe are modeled, and using state-of-the-art density functional theory with the group theory of solids, their symmetry-enforced electronic properties are studied. The in-plane ferroelectricity coupled with strong spin-orbit coupling induces a unidirectional out-of-plane Rashba spin-orbit field that can host a momentum-independent uniform spin configuration known as persistent spin texture (PST) at the Brillouin zone center. PST in these structures is found to be robust against external perturbations such as strain, structural distortion, and independent of layer thickness. These unprecedented intrinsic spin transport properties hold utmost importance in spintronics, as the experimental stringent condition of equal Rashba and Dresselhaus constants [Phys. Rev. Lett. **90**, 146801 (2003)] is eliminated. The calculated persistent spin helix wavelength of $<\sim 5$ nm paves the way for developing next-generation nanosized nonballistic spin field-effect transistors compared with micrometer-sized GaAs/AlGaAs quantum wells. Further, these materials exhibit finite spin Hall conductivity at the band edges and hence can be used in ferromagnet-free spin Hall transistors. Although CdTe and ZnTe systems have been widely studied for photocatalysis and solar cell applications over the past few decades, their potential application in spintronic devices has not been explored. Mono/few layers of CdTe and ZnTe synthesized from (110) facets of bulk zinc-blende crystals [Nat. Commun. **3**, 1057 (2012)] satisfy all symmetry operations of the nonsymmorphic space group and hence can be considered ideal materials to verify our theoretical results experimentally.

DOI: 10.1103/PhysRevB.108.085432

I. INTRODUCTION

The postgraphene era has witnessed the prediction, synthesis, and introduction of quantum materials with emergent functionalities where symmetry, topology, and dimensionality play an important role [1–4]. Electrons possess three degrees of freedom (DOFs): charge, spin, and valley. Controlling each DOF for data storage and manipulation leads to three specific research fields: electronics, spintronics, and valleytronics [5–9]. The spin and valley DOFs appear due to relativistic effects and can manifest in materials having strong spin-orbit coupling (SOC) and requiring certain conditions, such as broken inversion symmetry [10–12]. In recent years, there has been a surge of interest in manipulating spin DOFs at the nanoscale. Consequently, extensive theoretical and experimental investigations have been carried out, making the field of spintronics evolve [13–15].

The spin field-effect transistor (FET) consists of three components: source, drain, and semiconducting channel material. The source and drain are ferromagnetic materials having a particular spin orientation; the source injects the spin into the semiconducting channel material, and the drain detects the injected spin depending on its relative orientation [5,7,16]. The spin precession can be manipulated by applying an external perpendicular electric field. Recently, there have been experimental interests in redesigning/simplifying conventional spintronic devices; Zhu *et al.* [15] proposed semiconducting channel materials that show strong SOC, have a large out-of-plane piezoelectric coefficient, and are flexible so that piezopotential generated by channel material under strain can replace the external electric field. In this regard, Mohanta *et al.* [17] suggested hexagonal buckled CdTe and ZnTe monolayers which are direct band gap semiconductors and show significant out-of-plane piezoelectric coefficients. Further, these monolayers exhibit Rashba-type spin splitting at the conduction band minima (CBM) and hence are considered excellent channel material for next-generation strain-spintronic devices [18,19]. Another approach is to eliminate the intrinsic limitation of spintronic devices, such as short spin lifetime. In a diffusive transport regime, elastic/inelastic electron scattering from the defects and nonmagnetic impurity randomizes the spin due to the momentum-dependent spin-orbit field (SOF) $\Omega(k)$, which reduces the spin lifetime. The process is known as Dyakonov-Perel spin relaxation [20]. A way to circumvent this process is to make the magnitudes of Rashba and Dresselhaus constants equal [21,22], which can be realized in an experiment by controlling quantum well width and doping level [13,14,23–25]. SOC systems generally break the spin-rotation symmetry. However, SU(2) rotation symmetry is discovered under these conditions, stabilizing the periodic precession around the unidirectional SOF, known as a persistent spin helix (PSH) [26]. An overview of the PSH is discussed in Sec. II. Persistent spin texture (PST) has been previously observed in bulk systems such as $BiInO_3$ [27],

---

[*] manishkmr484@gmail.com, mohantamk@vcu.edu
[†] pjena@vcu.edu

$CsBiNb_2O_7$ [28], and quantum well structures [13,14,23,24]. Recently, only a few classes of two-dimensional (2D) monolayers have been proposed to support PST [29–32].

Alternatively, in recent theoretical work, Tao and Tsymbal [27] demonstrated that the stringent condition of equal Rashba and Dresselhaus constants can be overcome in bulk materials having nonsymmorphic space groups that exhibit intrinsic PST, enforced by symmetry. Nonsymmorphic crystal symmetries [33] combine a fractional lattice translation with either a mirror reflection (glide plane) or a rotation (screw axis), as schematically presented in Fig. S1 in the Supplemental Material (SM) [34]. The importance of nonsymmorphic crystal symmetry has been widely studied in topological materials, where the symmetry-enforced band crossing exists due to nonsymmorphic symmetries alone, independent of the material details [35–40]. In this paper, two nonsymmorphic crystal structures are modeled, and an in-depth analysis of their symmetry-enforced emergent properties is investigated.

II. THEORY OF PSH AND OUT-OF-PLANE SOF

A. Quantum mechanical perspective

The microscopic origin of the spin-orbit interaction in 2D semiconductors is the absence of inversion symmetry and confining potential. This results in Rashba and Dresselhaus (linear and cubic) spin-orbit terms in the effective Hamiltonian. In the Rashba effect, the spin degeneracy is lifted from SOC under inversion symmetry breaking. The Dresselhaus effect is present in semiconductors lacking bulk inversion symmetry such as in zinc-blende-type structures [41].

The effective SOC Hamiltonian can be written as

$$H_{\mathrm{SO}} = \tilde{\Omega}_{\mathrm{SOF}} \cdot \vec{\sigma}, \tag{1}$$

where $\tilde{\Omega}_{\mathrm{SOF}}$ is the SOF, and $\vec{\sigma}$ is the Pauli spin matrices. As confirmed experimentally, the cubic term in k only changes the strength of β in Eq. (2), leaving the Hamiltonian unchanged [42–44]. Thus, the general form of the Hamiltonian includes linear terms of both Rashba and Dresselhaus contributions for the 2D system and is given by [21,41,45]

$$\mathcal{H} = \frac{\hbar^2\, k^2}{2m} + \alpha(k_x\sigma_y - k_y\sigma_x) + \beta(k_y\sigma_y - k_x\sigma_x), \tag{2}$$

where $\vec{k}$ is the momentum of the electron confined in a 2D geometry, α and β correspond to the strengths of Rashba and Dresselhaus SOC, respectively, and m is the effective electron mass. The Rashba coefficient α is tunable using an external electric field perpendicular to the plane of the 2D electron gas, whereas the Dresselhaus constant β depends on the semiconductor material and the geometry of the sample.

The energy dispersion of this Hamiltonian leads to two branches:

$$\varepsilon_{\pm}(\vec{k}) = \frac{\hbar^2\, k^2}{2m} \pm \sqrt{(\alpha k_y + \beta k_x)^2 + (\alpha k_x + \beta k_y)^2}. \tag{3}$$

For zero value of coupling constants α or β, the dispersions are isotropic, and Fermi contours are concentric circles, whereas for nonzero α and β, the energy contour plots are anisotropic having (1,1) and (1,−1) directions as symmetry axes [46]. The spin rotation symmetry is generally broken in SOC systems. However, particularly for $\alpha = \pm\beta$, a type of special unitary SU(2) spin-rotation symmetry $\Sigma = (\sigma_x \pm \sigma_y)/\sqrt{2}$ is discovered that leaves the Hamiltonian invariant $[\mathcal{H}, \Sigma] = 0$ [22,26]. Under this condition, the spin-up and spin-down states of the electron become independent of the wave vector and hence prevent the randomization of the spin. The electron spin undergoes a controlled rotation known as the PSH. Additionally, previous investigators have indicated that, under certain relations between the Rashba constant and radius of curvature in a rolled-up 2D electron gas, tangential spin can be preserved [47].

The Hamiltonian can be formulated for $\alpha = \pm\beta$ as [22]

$$\mathcal{H} = \frac{\hbar^2}{2m}[k^2 + 2(\vec{k} \cdot \vec{Q})\Sigma]. \tag{4}$$

The energy dispersions form circles whose centers are displaced from the Γ point by shifting wave vector $\vec{Q}$:

$$\varepsilon_{\pm}(\vec{k}) = \frac{\hbar^2}{2m}[k^2 \pm 2(\vec{k} \cdot \vec{Q})]. \tag{5}$$

The spin-up and spin-down bands have an important shifting property [26]:

$$\varepsilon_{\downarrow}(\vec{k}) = \varepsilon_{\uparrow}(\vec{k} + \vec{Q}). \tag{6}$$

Authors of recent theoretical work [27] have suggested that PST can be imposed by symmetry, overcoming the condition of equal Rashba and Dresselhaus parameters. In this regard, a class of quantum materials having orthorhombic nonsymmorphic crystal structures such as SnTe, GeTe thin films, and Bi (110) exhibiting strong SOC and extra symmetries like glide-plane reflection symmetries have been proposed to realize an out-of-plane Rashba effect $\Omega^z_{\mathrm{SOF}}(\vec{k})$ [32,48,49]. In these materials, the in-plane electric field in a 2D electron system can generate a unidirectional SOF expressed by

$$\tilde{\Omega}_{\mathrm{SOF}}(\vec{k}) = \alpha(\hat{E} \times \vec{k}). \tag{7}$$

Application of the in-plane electric field $\vec{E}$ ($\hat{E}$ represents field direction) parallel to $\hat{x}$ yields a SOF with the following term:

$$\tilde{\Omega}_{\mathrm{SOF}}(\vec{k}) = \alpha(\hat{x} \times \vec{k}) = \alpha k_y \hat{z}. \tag{8}$$

This unidirectional perpendicular SOF, referred to as the out-of-plane Rashba effect, is induced by the in-plane electric field and has an identical form in the III-V quantum well grown along the [110] direction [21]. The Hamiltonian can be written as

$$\mathcal{H} = \mathcal{H}_{\mathrm{kin}} + \tilde{\Omega}_{\mathrm{SOF}}\vec{\sigma} = \frac{\hbar^2}{2m}\left(k_x^2 + k_y^2\right) + \alpha k_y \sigma_z. \tag{9}$$

For a ferroelectric material, built-in polarization generates the in-plane electric field, and hence, the SOF induced by the ferroelectric polarization (P) can be written as

$$\tilde{\Omega}_{\mathrm{SOF}}(\vec{k}) = \alpha(\hat{P} \times \vec{k}), \tag{10}$$

where $\hat{P}$ is the direction of ferroelectric polarization that replaces $\hat{E}$ in Eq. (7).

B. Group theory perspective

In recent work, Tao and Tsymbal [27] have demonstrated that the PSH can be an intrinsic property of a material if it belongs to a nonsymmorphic space group crystal structure.

TABLE I. Transformation rules for wave vector (k), Pauli matrices (σ) under time-reversal symmetry, implying a reversal of both spin and momentum ($\hat{T}$) and C_{2v} point group symmetry operation $\hat{C}_{2x}$, $\hat{M}_{xy}$, $\hat{M}_{zx}$ for the Γ point in the first BZ.

Symmetry operation	(k_x, k_y)	$(\sigma_x, \sigma_y, \sigma_z)$
$\hat{T} = i\sigma_y K$; K is complex conjugation	$(-k_x, -k_y)$	$(-\sigma_x, -\sigma_y, -\sigma_z)$
$\hat{C}_{2x}$	$(k_x, -k_y)$	$(\sigma_x, -\sigma_y, -\sigma_z)$
$\hat{M}_{xy}$	(k_x, k_y)	$(-\sigma_x, -\sigma_y, \sigma_z)$
$\hat{M}_{zx}$	$(k_x, -k_y)$	$(-\sigma_x, \sigma_y, -\sigma_z)$

In general, the symmetry operations of the nonsymmorphic space group No. 31 are given by

$$\left\{\langle Ee|\{0,\ 0,\ 0\}\rangle,\ \langle C_{2z}|\left\{\tfrac{1}{2}, 0, \tfrac{1}{2}\right\}\rangle,\ \langle IC_{2y}|\left\{\tfrac{1}{2}, 0, \tfrac{1}{2}\right\}\rangle,\ \langle IC_{2x}|\{0, 0, 0\}\rangle\right\}. \tag{11}$$

The twofold rotations followed by inversion symmetry (IC_{2y}) leads to mirror-reflection symmetry ($\hat{M}_{zx}$), and hence, the terms in Eq. (11) can be written as

$$\{E,\ \hat{C}_{2z},\ \hat{M}_{zx},\ \hat{M}_{yz}\} \tag{12}$$

Here, the translational terms are excluded. A more detailed explanation of symmetry operations is provided in Table S1 in the SM [34].

Since the PSH has been shown to originate from SU(2) rotational symmetry in earlier work [26] and from crystal symmetry [27], a one-to-one correlation between a rotational symmetry operation in SU(2) and the crystallographic point group must exist. Here, SU(2) is a group of unitary matrices and has three generators: { $i\sigma_x$, $i\sigma_y$, $i\sigma_z$ } (see Secs. S1 and S2 in the SM for more details [34]).

The crystal structure of the 2D nonsymmorphic space group is invariant under several point group operations {E, $\hat{C}_{2x}$, $\hat{M}_{zx}$, $\hat{M}_{xy}$}, which takes similar form to that of Eq. (12) [31]. Considering transformation rules in Table I and the C_{2v} point group symmetry operation, it can be shown that the unidirectional SOF is protected by M_{xy}, as Ω^z_{SOF} survives under the in-plane mirror reflection, whereas Ω^z_{SOF} becomes an odd function under the vertical mirror reflection M_{zx}: $\Omega^z_{\mathrm{SOF}}(k_x, -k_y) = -\Omega^z_{\mathrm{SOF}}(k_x, k_y)$ [32].

III. RESULTS AND DISCUSSION

A. Atomistic modeling of ideal nonsymmorphic 2D crystal structures, symmetry analysis, and stability

Using the group theory of solids supported by density functional theory (DFT) results, Tao and Tsymbal [27] have demonstrated that intrinsic PST can be enforced by nonsymmorphic space group symmetry in certain bulk materials. Following previous reports, two-atom thick nonsymmorphic crystal structures composed of Cd-Te and Zn-Te have been modeled using the same bond length and bond angles between the atoms as that of respective bulk zinc-blende crystal structures [50]. The same approach has been adopted in earlier work [27] for analyzing the symmetry-enforced properties excluding any additional effects from structural perturbation.

TABLE II. Geometrical parameters of modeled nonsymmorphic structures: lattice constants a, b; bond length (a_1, a_2), and bond angle (θ_1, θ_2); the vertical distance between atomic layers (d).

Systems	a (Å)	b (Å)	$a_1 = a_2$ (Å)	$\theta_1 = \theta_2$ (deg)	d (Å)
Orthorhombic CdTe (o-CdTe)	6.56	4.64	2.84	109.47	2.32
Orthorhombic ZnTe (o-ZnTe)	6.11	4.32	2.64	109.47	2.16

Particularly, CdTe and ZnTe are considered for modeling in this paper, as Mohanta *et al.* [17] have recently reported Rashba spin splitting in CdTe and ZnTe hexagonal buckled structures. The ideal nonsymmorphic structures are modeled to generalize the properties originating from crystal symmetry, and thus, thickness dependance is excluded. Detailed geometrical parameters of our designed structures are listed in Table II. Each unit cell contains four atoms having four symmetry operators that leave the atomic configurations invariant: (i) identity operation E; (ii) twofold screw rotation $\bar{C}_{2x}$ (twofold rotation around the x axis, $\hat{C}_{2x}$, followed by a translation of $\tau = \frac{a}{2}, \frac{b}{2}$), where a and b are the lattice parameters along the x and y axes, respectively; (iii) glide reflection (G or $\bar{M}_{xy}$; reflection with respect to the xy plane followed by translation τ); and (iv) reflection M_{zx} with respect to the zx plane. The top and side views of the nonsymmorphic CdTe and ZnTe crystal structures along with mirror (M_{zx}) and glide reflection (G) symmetries are indicated in Fig. 1. The designed crystal structures exhibit nonsymmorphic symmetry through a glide-mirror operation; reflection about the $z = 0$ plane (M_{xy})

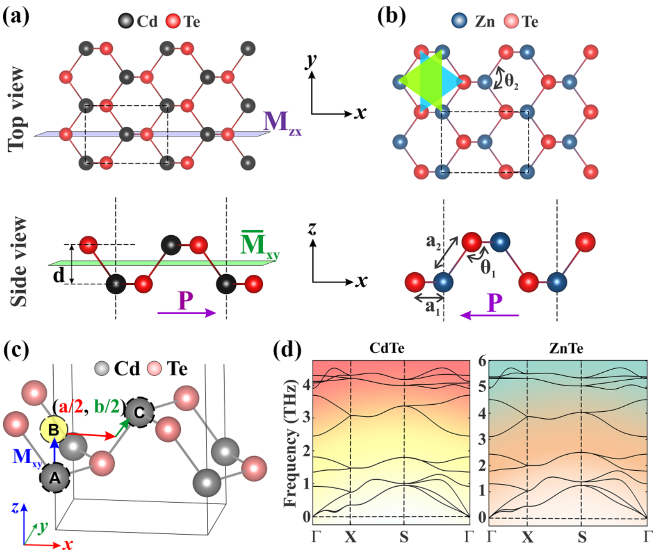

FIG. 1. (a) and (b) Top and side views of designed two-dimensional (2D) nonsymmorphic CdTe and ZnTe crystal structures; the unit cell is marked by a dashed line, mirror symmetry M_{zx}, glide plane symmetry G or $\bar{M}_{xy}$, and direction of ferroelectric polarization in the unit cell is indicated. (c) Illustration of a nonsymmorphic group operation on CdTe modeled structure includes mirror reflection A → B and a translation B → C. (d) Phonon dispersion plot of CdTe and ZnTe along the high-symmetry direction of the rectangular Brillouin zone; Γ (0,0,0)→X (0.5,0,0)→S (0.5,0.5,0)→ Γ(0,0,0).

followed by a translation of $a/2$ and $b/2$ along the x and y axes, respectively. As illustrated in Fig. 1(c), starting from the Cd at atomic site A, mirror reflection (M_{xy}) brings it to site B, which is not allowed in the structure. An additional fractional translation t: $(a/2, b/2, 0)$ is needed to bring it to the allowed atomic site C. As can be seen from the top view in Fig. 1, the relative positions of the constituent atoms with respect to the crystal axis are opposite in CdTe and ZnTe unit cells, and hence, the ferroelectric polarization directions will be opposite to each other, which will be discussed later. The nonsymmorphic groups are more numerous than the symmorphic groups, and these crystals extensively occur in nature. For example, the diamond crystal structure belongs to the nonsymmorphic space group. Recently, several monolayers having nonsymmorphic crystal symmetry have been proposed and synthesized: phosphorene [51], SnS, SnSe, GeS, GeSe [52], SnTe monolayer [53], GeTe [54], Bi (110) monolayer [48,55], and group-VA [56].

To check the dynamical stability of the unit cells, phonon dispersions of both structures are plotted in Fig. 1(d). The vibration of four atoms in the unit cell leads to twelve phonon modes out of which three are acoustic and nine are optical phonon branches. The positive phonon frequency of both acoustic and optical modes indicates that the bonds between the atoms have sufficient restoring force to retain their original symmetry, bond length, and bond angles, thus confirming their structural stability. Since the designed structures are stable, a systematic investigation of electronic properties has been conducted to shed light on (i) the intrinsic PSH in these 2D structures enforced by symmetry, (ii) the effect of ferroelectric switching/polarization ($\pm P$) on spin polarization, (iii) the effect of external perturbations such as vertical electric field and biaxial strain on PST, and (iv) the feasibility of experimental realization and application in a spin Hall effect (SHE) transistor.

B. Ferroelectric polarization and spatial inversion operator

The ferroelectricity is originated from noncentrosymmetric symmetry, as indicated by colored triangles in Fig. 1(b), and a nonsymmorphic element in the crystal structure which breaks the local structural mirror symmetry and forms a dipole moment. The directions of ferroelectric polarization ($\vec{P}$) are opposite each other in CdTe ($+x$) and ZnTe ($-x$). For a 2D system, under a spatial inversion operator or a C_{2z} operator (180° rotation around the z axis), the wave vector transformed as $(k_x, k_y) \xrightarrow{I} (-k_x, -k_y)$, as does the ferroelectric polarization $\vec{P} \xrightarrow{I} -\vec{P}$ [29,57] (see Fig. 2). The magnitudes of the in-plane ferroelectric polarization in the unit cell are calculated to be 2.22×10^{-10} C/m and 2.32×10^{-10} C/m for CdTe and ZnTe, respectively, which are comparable with other ferroelectric 2D materials: functionalized MXenes (4.93×10^{-10} to 6.25×10^{-10} C/m) [58], In_2Se_3 (2.59×10^{-10} C/m) [59], GeS (5×10^{-10} C/m) [60], and Bi(110) monolayer (0.47×10^{-10} C/m) [48].

C. Electronic properties with and without SOC

The electronic band structure of nonsymmorphic CdTe and ZnTe are plotted in Fig. 3. From the electronic band dispersion, these materials are found to be direct band gap semiconductors with band edges, the CBM and valence band maxima (VBM) located at the Brillouin zone (BZ) center. The atom-projected band structure indicates that the VBM is mainly contributed by Te atoms, whereas the CBM is contributed by both Cd and Te atoms, which can be confirmed from the band-decomposed charge density plot in Fig. 3. The band gaps obtained using different functionals are listed in Table III. These values indicate that the band gap lies in the visible region and is comparable with the values in well-known MoS_2 (~1.8 eV) [4,67] and WS_2 (~2.1 eV) [68]. Hence, these materials can have the potential for electronics and optoelectronics applications. Previously, CdTe and ZnTe monolayers/thin films of different geometry had been extensively studied for solar cell and catalysis applications [69–75].

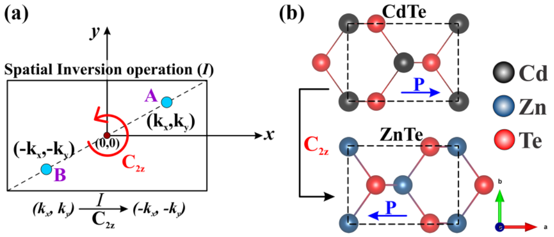

FIG. 2. (a) Schematic representation of spatial inversion operation in a two-dimensional (2D) system $I(k_x, k_y) \rightarrow (-k_x, -k_y)$; point B is the final position of point A under spatial inversion operation (**I**) which can be obtained by a C_{2z} symmetry operation in the crystal structure. (b) Illustration of spatial inversion symmetry and direction of ferroelectric polarization ($\vec{P}$); $\vec{P} \rightarrow^{I/C_{2z}} -\vec{P}$.

Further, since both these structures contain heavy tellurium atoms, the relativistic effect is incorporated in the electronic properties calculation, and the spin-projected band structure is plotted in Fig. 4. The effect of SOC can be observed in the band dispersion plot as the band gap decreases (refer to Table III). There are two very interesting notable observations in the band structure: (i) Rashba-type spin splitting occurs at both CBM and VBM, and (ii) the spin splitting occurs along the $\Gamma \rightarrow Y$ direction, whereas the spin states remain degenerate along the $\Gamma \rightarrow X$ line. The first observation can be explained by the orbital contributions of band edges and the direction of ferroelectric polarization in the system. From the orbital projected band structure in Fig. 3, the band edges are confirmed to be contributed by in-plane Cd d_{xy} and Te p_x atomic orbitals, and the ferroelectric polarization is along the $+x$ axis (P_x/E_x). Hence, the Rashba-type spin splitting is observed in both CBM and VBM: $\langle d_{xy}|E_x|d_{xy}\rangle \neq 0$ and $\langle p_x|E_x|p_x\rangle \neq 0$ [17,19,63].

Now the origin of the degenerate state along the $\Gamma \rightarrow X$ line in the presence of SOC can be explained using the symmetry of the wave vector $\vec{k}$, which is invariant under $\bar{C}_{2x}$ screw rotation and $\bar{M}_{xy}$ glide mirror-reflection symmetry. Since the Pauli matrices are anticommutative $\{\sigma_x, \sigma_z\} = 0$ in nature, the operators (refer to Eq. (s4) in the SM [34]) follow the same: $\{\bar{C}_{2x}, \bar{M}_{xy}\} = \{i\sigma_x,\ i\sigma_z\} = 0$ on the line $\Gamma \rightarrow X$. Now for an eigenvector $|\psi_m\rangle$ of $\bar{M}_{xy}$ operator with the eigenvalue of m the following can be obtained:

$$\bar{M}_{xy}|\psi_m\rangle = m|\psi_m\rangle, \tag{13}$$

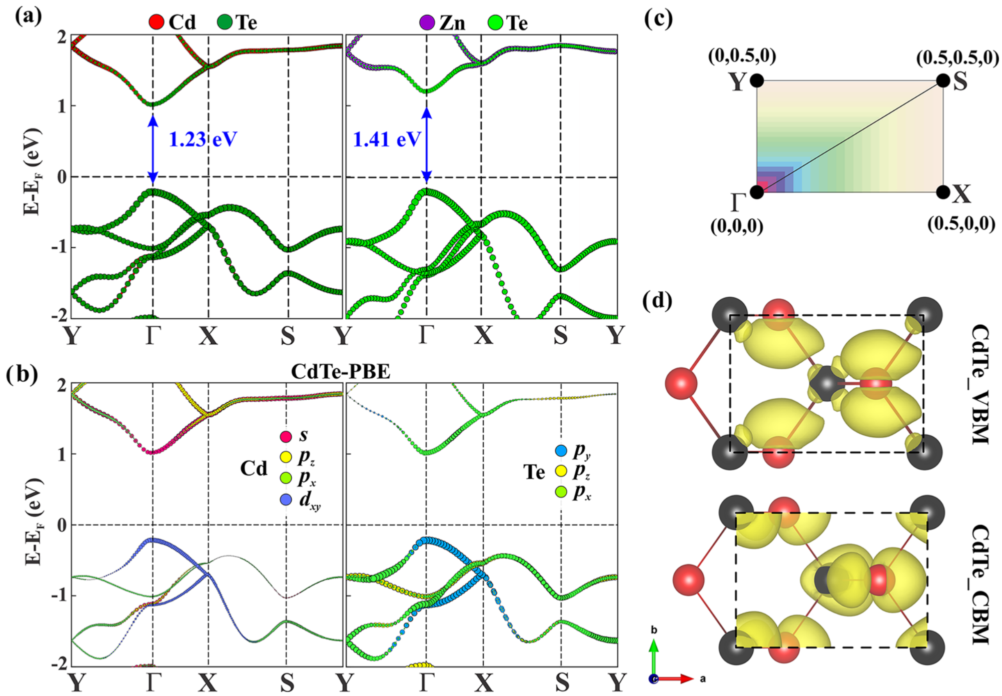

FIG. 3. (a) Calculated atom-projected electronic band dispersion of CdTe and ZnTe two-dimensional (2D) structures using GGA-PBE. (b) Orbital projected band structure of CdTe. (c) Schematic of Brillouin zone of a rectangular unit cell. (d) Band decomposed charge density of CdTe corresponding to band edges with an isosurface value of 0.0025 e/Å^3.

$$\bar{M}_{xy}\bar{C}_{2x}(|\psi_m\rangle) = -\bar{C}_{2x}\bar{M}_{xy}|\psi_m\rangle = -m\bar{C}_{2x}|\psi_m\rangle = -m\,(\bar{C}_{2x}|\psi_m\rangle). \tag{14}$$

Equations (13) and (14) indicate that $|\psi_m\rangle$ and $\bar{C}_{2x}|\psi_m\rangle$ are different states with the same eigenvalue m, thus ensuring the double degeneracy along the $\Gamma \rightarrow X$ line.

Also, the same result can be obtained using Eq. (10), the Rashba SOF $\tilde{\Omega}_{\mathrm{SOF}}(\vec{k}) = \alpha(\pm\hat{P}_x \times \vec{k}_x) = 0$ along the $\Gamma \rightarrow X$ line. Here, $\pm\hat{P}_x$ corresponds to the polarization direction in CdTe and ZnTe structures, respectively.

TABLE III. Calculated band gap of o-CdTe and o-ZnTe using different functionals.

System	E_g^{PBE} (eV)	$E_g^{\mathrm{PBE+SOC}}$ (eV)	E_g^{HSE} (eV)	$\Gamma \rightarrow Y$ α_R^{CBM} (eV Å)	α_R^{VBM} (eV Å)
o-CdTe	1.23	1.14	1.81	1.35	1.77
o-ZnTe	1.41	1.33	2.1	1.37	1.79
Reported Rashba constant values of other 2D materials for comparison					
2D materials				CBM	VBM
Buckled CdTe [17]				1.27	/
Buckled ZnTe [17]				1.06	/
BiSb [61]				2.3	/
WA$_2$Z$_4$ [62]				/	0.87–1.8
AlBi [63]				2.77	/
WSeTe [64]				/	0.92
PtSe$_2$/MoSe$_2$ [65] heterostructure				/	1.3
BiTeX [66]				1.86	/

The energy eigenvalues of the effective Hamiltonian of the 2D system presented in Eq. (9), i.e., $H = E_0(k) + \alpha k_y \sigma_z$ are given by [76]

$$E^{\pm}(k) = E_0(k) \pm \alpha k_y. \tag{15}$$

Equation (15) represents the spin splitting along $\Gamma \rightarrow Y$ directions and also leads to the following shifting property: $\varepsilon_{\downarrow}(\vec{k}) = \varepsilon_{\uparrow}(\vec{k} + \vec{Q})$, where $\vec{Q}$ is the shifting wave vector given

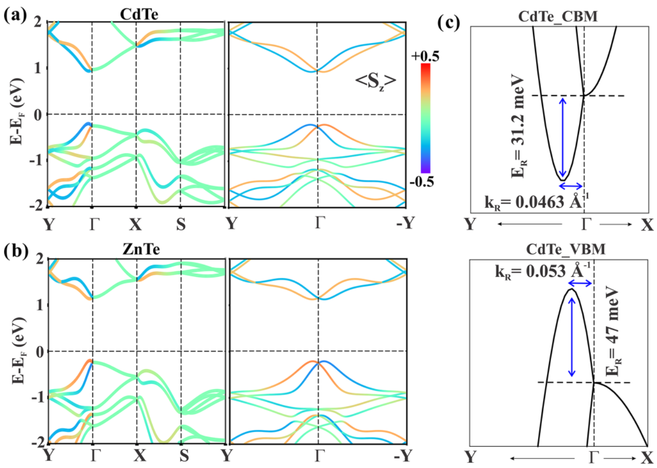

FIG. 4. (a) and (b) Spin-projected electronic band structure of CdTe and ZnTe including relativistic effect. (c) Zoomed image of conduction band minima (CBM) and valence band maxima (VBM) of CdTe at the Γ point.

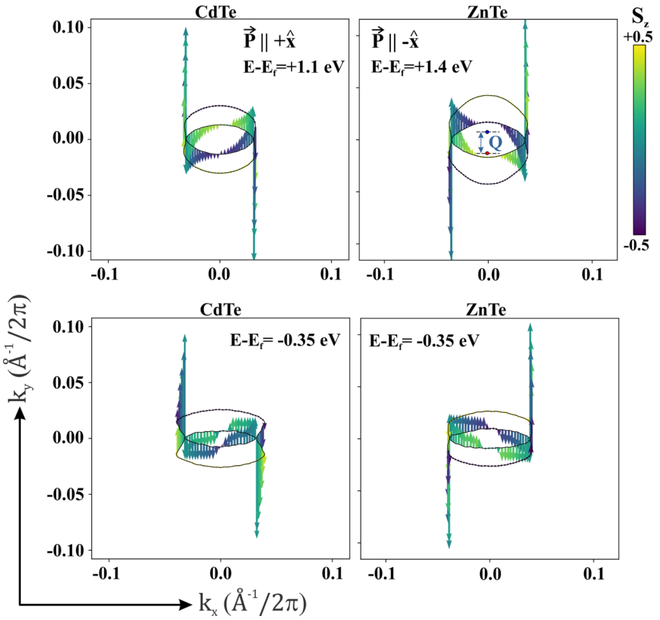

FIG. 5. Spin-projected constant energy contour plots of spin texture calculated in k_x-k_y plane centered at the Γ point; reference Fermi energy is zero. The arrow represents spin-polarization direction $\pm z$.

by

$$\vec{Q} = \frac{2m_y^*\alpha}{\hbar^2}[0, 1, 0]. \tag{16}$$

Here, m_y^* is the effective mass of an electron along the $\Gamma \rightarrow Y$ direction, and α is the Rashba constant. The shifting wave vector can be depicted in Fig. 5. The strength of SOC known as the Rashba parameter (α) along the $\Gamma \rightarrow Y$ direction can be calculated from the band dispersion using Eq. (17) (the results are listed in Table III):

$$\alpha = \frac{2E_R}{k_R}. \tag{17}$$

Here, E_R is the energy difference between the energies at the peak and the high-symmetry point, and k_R is the momentum offset between the peak and the high-symmetry point as marked in Fig. 4(c). The calculated value of the Rashba constant is nearly the same for both CdTe and ZnTe. For comparison, a list of Rashba constant values of other 2D Rashba materials is provided in Table III.

Now to visualize the spin-polarization direction in the designed structures, the spin texture is plotted at a constant energy above and below the Fermi level in Fig. 5, which indicates its unidirectional (S_z) nature. Note that the ferroelectric polarization directions are opposite in CdTe and ZnTe, as discussed in Sec. III B. Comparison of the spin texture plots provides a qualitative understanding of the relationship between the spin-polarization direction and ferroelectric polarization. This can be explained in two ways [29,57]:

(i) Let the Bloch wave functions of two states with opposite ferroelectric polarization be represented by $|+P, k\rangle$ and $|-P, k'\rangle$, where P and k are the ferroelectric polarization and wave vector, respectively. Considering the wave function $|+P, k\rangle$, the transformation under spatial inversion symmetry (I) is given by $I|+P, k\rangle = |-P, -k\rangle$, where both ferroelectric polarization and wave vector reversed their directions. Under time-reversal symmetry ($\hat{T}$), the wave function transformed to $\hat{T}|+P, k\rangle = |+P, -k\rangle$, where the direction of ferroelectric polarization remains intact. Here, time-reversal symmetry is included since the spin reverses its direction (spin-up and spin-down) under the time-reversal operator. Some properties of the time-reversal symmetry operator $\hat{T}$ are listed in Table S2 in the SM [34]. Now under both time-reversal and inversion symmetry, the given wave function is transformed to $\hat{T}I|+P, k\rangle = |-P, k\rangle$. Considering these transformation rules, the behavior of the spin-polarization direction with ferroelectric polarization can be explained. The expectation value of the spin operator $\langle S\rangle$ can be obtained as follows [29,57]:

$$\begin{aligned}\langle S\rangle[-P, k] &= \langle -P, k|S| - P, k\rangle = \langle +P, k|I^{-1}T^{-1}STI|+P, k\rangle \\ &= \langle +P, k| - S| + P, k\rangle = \langle -S\rangle[+P, k]. \end{aligned} \tag{18}$$

Equation (18) clearly describes the reversible spin-polarization direction by ferroelectric switching using symmetry analysis.

(ii) Also, the orientation of spin texture with the direction of polarization can be directly obtained from Eq. (10):

$$\text{For } +\hat{P}: \ \tilde{\Omega}_{\text{SOF}}(\vec{k}) = \alpha(+\hat{P} \times \vec{k}) = \alpha k_y(+\hat{z}) \tag{19}$$

$$\text{For } -\hat{P}: \ \tilde{\Omega}_{\text{SOF}}(\vec{k}) = \alpha(-\hat{P} \times \vec{k}) = \alpha k_y(-\hat{z}). \tag{20}$$

Equations (19) and (20) indicate the reversible nature of spin orientation with ferroelectric polarization, as demonstrated in Figs. 4 and 5. Note that authors of recent experimental work have demonstrated purely in-plane ferroelectricity at room temperature in monolayer SnS [77], which has a similar crystal structure.

The spatially periodic mode of the PSH, also known as the pitch/wavelength of the PSH, can be calculated using the following relation:

$$l_{\text{PSH}} \equiv \frac{2\pi}{|\vec{Q}|} = \frac{\pi\hbar^2}{m_y^*\alpha}. \tag{21}$$

For practical application of the out-of-plane Rashba effect, the coherent spin precession of the PSH can be used to fabricate a spin transistor with a size that is determined by l_{PSH} [22,32,78]. The short pitch size of a rapidly precessing PSH is highly desirable. All the variables for the calculation of l_{PSH} are listed in Table IV and are found to be ∼4 and 5 nm for o-CdTe and o-ZnTe, respectively. To design ultrathin spin-FET having a channel length of l_{PSH}, a material having a large Rashba coefficient (α) is required. Therefore, the 2D ferroelectric materials consisting of heavy elements that possess large atomic SOC are of interest.

D. Effect of vertical electric field on PSH and spin Hall transistor

Next, the effect of external perturbations such as perpendicular electric field and biaxial strains on electronic properties are studied. A vertical electric field is applied perpendicular to the plane of the 2D structures. The resulting band gap variation is plotted in Fig. 6(a). Although there is a slight decrease in the band gap with increasing electric field, beyond the critical field of 0.3 V/Å for both CdTe and ZnTe,

TABLE IV. Calculated effective mass of the electron, Rashba constant, and the pitch of PSH (l_{PSH}) of the conduction band.

Systems	Effective mass of the electron m^*/m_0 along $\Gamma \rightarrow Y$	Rashba constant (α) (eV.Å)	l_{PSH}
o-CdTe (thickness 2.32 Å)	0.392	1.35	4.5 nm
o-ZnTe	0.442	1.37	3.9 nm
$BiInO_3$ bulk [27]	0.61	1.91	2 nm
SnTe (001) thin film [32]	/	/	8.8–18.3 nm
GaAs/AlGaAs (001) quantum wire [23]	/	/	7–10 μm

near free electron gas states appear in the band structure that close the band gap. These states are surface-induced unoccupied empty states, parabolic, and move toward the Fermi level with increasing electric field at the Γ point, as seen in other 2D systems [79,80]. For a nonzero vertical electric field, the out-of-plane spin polarization is significantly affected, which leads to spin decoherence and can be depicted in Fig. 6(c). The complications in the spin texture plot arise because of the addition of a new perturbation term in the Hamiltonian which leads to different energy.

Further, the spin Hall conductivity (SHC) is calculated for both 2*L*-CdTe and ZnTe structures and plotted in Fig. 7(a). A finite SHC can be observed at the band edges. Motivated by previous reports [49,81] and based on our results, a spin Hall transistor (SHT) [82–84] is proposed, as illustrated in Fig. 7(b). The SHT device has three regions R-I, R-II, and R-III, which represent spin-injection, gate-controlled, and spin-collector regions, respectively. The spin from R-I can be injected into R-II via the SHE, where the charge current along the *y* direction is converted into a transverse spin current polarized along the *z* axis. In R-II, the out-of-plane SOF induces the PSH mode in the crystal, which can be modulated using a vertical electric field (E_z) applied using the gate electrode. For $E_z = 0$, the PSH mode is maintained, and hence, the polarized spins do not lose the spin information collected in R-III. Using the inverse SHE, the spin current is converted back into charge current along the *y* direction, which generates the Hall voltage as schematically presented in Fig. 7(b). For nonzero E_z in R-II, the spin decoherence occurs, which reduces the spin lifetime. Hence, the Hall voltage decreases. In other words, the PSH mode can be broken via nonzero vertical electric field.

E. Effect of biaxial strain on PST

Strain engineering can be an effective tool to manipulate the electronic properties such as the semiconducting-to

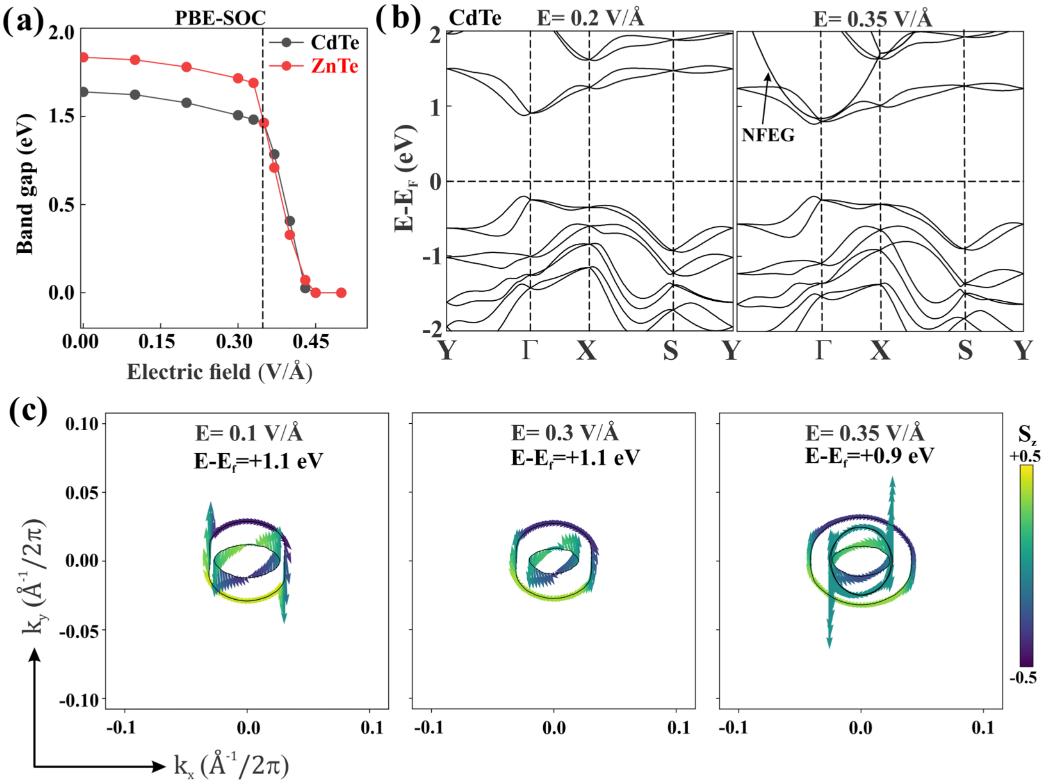

FIG. 6. (a) Calculated band gap variation under perpendicular electric field, (b) band dispersion, and (c) evolution of spin-texture plot of CdTe under different electric field strength.

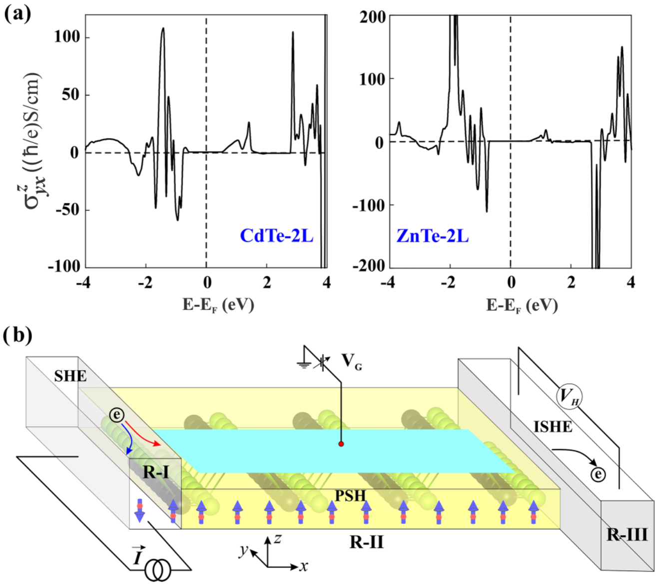

FIG. 7. (a) Calculated spin Hall conductivity for 2L-CdTe and ZnTe. (b) Schematic of a spin Hall effect transistor.

-metallic or direct-to-indirect band gap transformations [85–88], and it is possible using different experimental techniques such as AFM tips, bending on a flexible substrate, or interfacial lattice mismatch [89–92]. In this regard, a small biaxial strain of up to ±5% is applied, and electronic properties under strain are studied. Strain is defined as $\epsilon = \frac{a-a_0}{a_0}$, where a_0 and a are the unstrained and strained lattice constants, respectively. From the electronic dispersion plotted in Fig. 8(a), a significant change in the band gap as well as the spin splitting is observed. The band gap increases and decreases under compressive and tensile strain, respectively. The linear variation of the Rashba constant calculated from the band dispersion under biaxial strain is observed in Fig. 8(b). Hence, the magnitude of out-of-plane SOF, which depends on the Rashba constant as in Eq. (8): $\tilde{\Omega}_{\rm SOF}(\vec{k}) = \alpha k_y \hat{z}$, can be manipulated. Nevertheless, the PST is found to be robust against biaxial strain.

Next, the dependency of spin-transport properties on layer thickness and crystal structures having different symmetry are studied and depicted in Fig. 9. With increasing the layer thickness, the band gap decreases significantly, but the PST state enforced by unidirectional SOF is maintained in the system, and the same can be seen in the spin-projected band structure plot in Fig. 9(b). The other crystal structures such as hexagonal systems do not exhibit PST. Although hexagonal planar CdTe monolayers do not show any spin-dependent properties, buckled structures exhibit Rashba splitting at the CBM due to the built-in out-of-plane electric field E_z in the system coupled with p_z orbitals, i.e., $\langle p_z|E_z|p_z\rangle \neq 0$ [17,19,63]. Finite out-of-plane spin-polarized splitting occurs at the high-symmetry K point in a hexagonal buckled crystal structure. Such spin splitting is called valley spin splitting, which has been identified in previous work [19] on a similar system. The working principle of valleytronics is very different from spintronics and can be found elsewhere [10,93].

F. Effect of deformed crystal structure on PST and experimental realization

In the previous sections, 2D nonsymmorphic structures of CdTe and ZnTe have been modeled and proposed to exhibit many interesting symmetry-enforced properties such as intrinsic PST, band degeneracy, and reversible spin-polarization via ferroelectric switching (±P). These results have been explained using symmetry analysis supported by DFT calculations. To realize these unprecedented properties experimentally, (110) facets of bulk zinc-blende CdTe and ZnTe structures would be ideal to study, as the symmetry of this growth direction of the crystal structure is invariant under nonsymmorphic space group operations. In the previous experiment, highly stable four-atomic thick layers (4L) from (110) facets of the zinc-blende structure were exfoliated using a strategy involving a lamellar hybrid intermediate [94]. Authors of experimental work have confirmed that the ZnSe single layers possess a highly (110)-preferred orientation and are highly stable at room temperature. Although there is structural distortion at the surface of the experimentally synthesized monolayers to minimize the surface energy, it will be interesting to study whether the PSH can survive under such mechanical deformation. Since CdTe and ZnTe bulk structures are non-van der Waal solids, structural distortion of monolayer or a few layers at the surface is inevitable, as experimentally found in the case of three-atomic (3L) [95,96] and four-atomic (4L) thick layers [94]. A 4L layer is cleaved from the (110) plane of zinc-blend CdTe, and the atomic positions are relaxed. The side view of optimized structures is shown

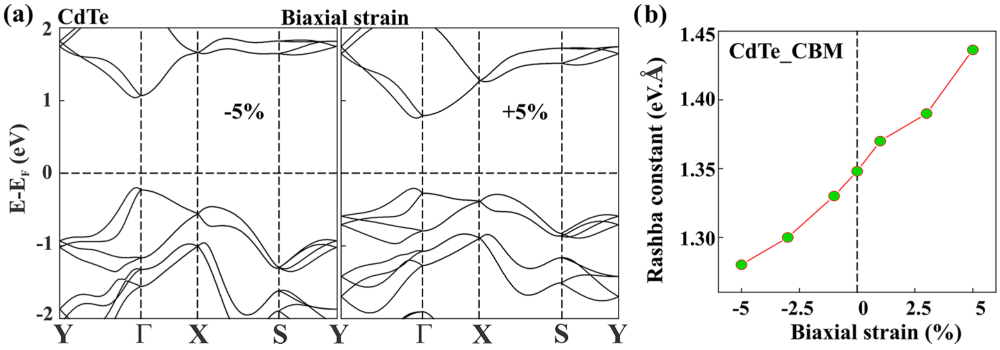

FIG. 8. (a) Calculated band dispersion of CdTe under biaxial strain. (b) Variation of the Rashba constant under biaxial strain.

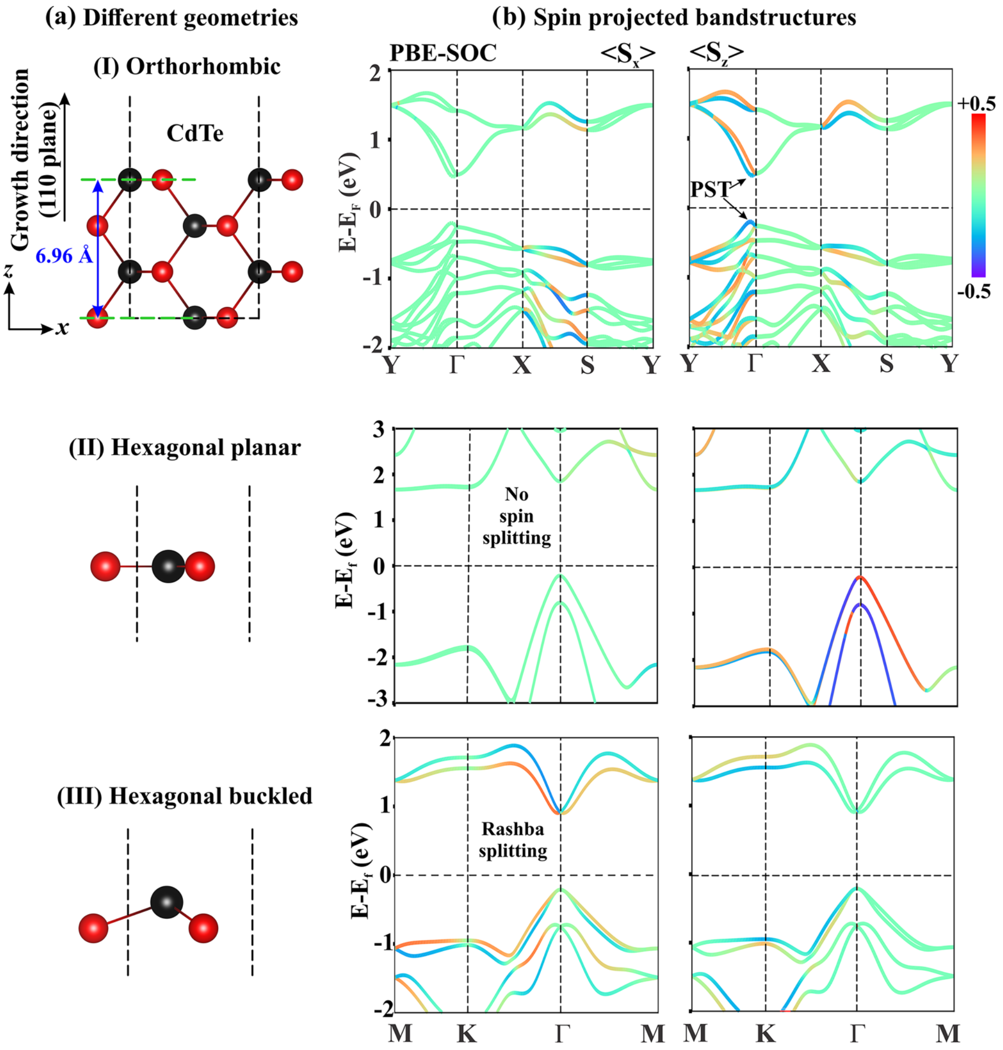

FIG. 9. Comparative plot of (a) different atomic arrangement of CdTe in the unit cell and (b) corresponding spin-projected S_x and S_z band structure.

in Fig. 10, which replicates the distorted structure reported in Ref. [94]. The electronic properties are evaluated considering the SOC, and the band structure is plotted in Fig. 10. The band edges are located at the BZ center, and the spin splitting along the $\Gamma \rightarrow Y$ direction remains unchanged. These results indicate (110) facets of zinc-blende structures of CdTe and ZnTe, as presented in Fig. S2 in the SM [34], are ideal materials for realizing the intrinsic PSH and thus realizing atomic thin nonballistic spin FET. Further, these results indicate that symmetry-enforced properties are globally stable and can survive under large mechanical deformation.

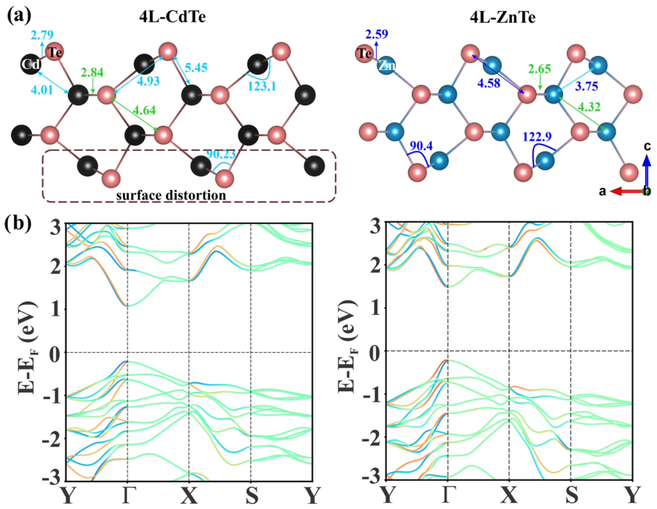

FIG. 10. (a) Side view of 4-atom thick (4L) CdTe and ZnTe structures replicating freestanding ZnSe synthesized from (110) facets of zinc-blende bulk crystal structure as in Ref. [94] and (b) their electronic band structure incorporating a relativistic effect.

IV. CONCLUSIONS

In conclusion, two-atomic thick nonsymmorphic crystal structures of CdTe and ZnTe are modeled in this paper. These structures exhibit many interesting electronic properties originated from symmetry such as momentum-independent uniform spin polarization, which leads to a long spin lifetime, and the reversible spin polarization via the ferroelectric switching. The pitch of the PSH is calculated to be ∼4−5 nm, and hence, an ultrathin nonballistic spin FET can be designed. The PST in these structures was found to be robust against strain, layer thickness, and structural distortion. However, the PSH mode can be broken via a nonzero vertical electric field. A finite SHC at the band edges with such intriguing electronic properties can motivate experimentalists to design a ferromagnet-free SHE transistor. Moreover, infinite spin lifetime in (110) facets of centuries-old tellurium-based zinc-blende semiconductors have been predicted in this paper using the group theory of solids supported by DFT and thus pave the way for the beginning of a new era in the field of spintronics.

V. COMPUTATIONAL DETAILS

All calculations are performed using DFT embedded in the VASP code [97,98]. The generalized gradient approximation (GGA) with Perdew-Burke-Ernzerhof (PBE) exchange-correlation interaction is used [99]. The projector augmented-plane-waves approach is employed to treat the ion-electron interaction [100]. The energy cutoff is set to 500 eV, and the energy convergence is set to 10^{-8} eV. To obtain experimental geometries of 4L CdTe and ZnTe as in Fig. 10, symmetry-constrained geometrical optimization is performed until the maximum force converges to 0.02 eV/Å. The BZ is sampled with a $14 \times 14 \times 1$ Γ-centered k-point mesh. A vacuum space of 20 Å is added in the z direction to eliminate periodic interaction between the layers. The second-order force constants are calculated using a $5 \times 5 \times 1$ supercell sampled with $10 \times 10 \times 1$ k-mesh using the finite difference method and plotted using the PHONOPY package [101]. PYPROCAR is used to plot spin texture [102]. The ferroelectric properties are calculated using the Berry phase method [103–105]. The SHC is calculated from Berry curvature using a dense $200 \times 200 \times 1$ k-mesh based on a maximally localized Wannier function [106–111] by the formula [112]:

$$\sigma^z_{xy} = \frac{e}{\hbar}\int_{Bz}\frac{dk}{(2\pi)^2}\Omega^z(k),$$

where $\Omega^z(k)$ is the k-resolved term which is given by $\Omega^z(k) = \sum_n f_{kn}\Omega^z_n(k)$. Here, f_{kn} is the Fermi-Dirac distribution function for the nth band at k, and $\Omega^z_n(k)$ is an analog of the Berry curvature for the nth band given as

$$\Omega^z_n(k) = \sum_{n'\neq n}\frac{2\mathrm{Im}\left[\langle kn|j^z_x|kn'\rangle\langle kn'|v_y|kn\rangle\right]}{(\epsilon_{kn}-\epsilon_{kn'})^2}.$$

Here, $j^z_x = \frac{1}{2}\{s_z, v\}$ is the spin-current operator, $s_z = \frac{\hbar}{2}\sigma^z$ is the spin operator, v is the velocity operator, and $|kn\rangle$ is the wave function of energy ϵ_{kn}.

ACKNOWLEDGMENTS

M.K.M and P.J. acknowledge financial support from the U.S. Department of Energy, Office of Basic Energy Sciences, Division of Materials Sciences and Engineering under Award No. DE-FG02-96ER45579. Resources of the National Energy Research Scientific Computing Center supported by the Office of Science of the U.S. Department of Energy under Contract No. DE-AC02-05CH11231 are also acknowledged. The authors extend their acknowledgment to the High-Performance Research Computing core facility at Virginia Commonwealth University for providing supercomputing resources.

---

[1] X.-L. Qi and S.-C. Zhang, Topological insulators and superconductors, Rev. Mod. Phys. **83**, 1057 (2011).

[2] F. Tang, H. C. Po, A. Vishwanath, and X. Wan, Comprehensive search for topological materials using symmetry indicators, Nature (London) **566**, 486 (2019).

[3] K. S. Novoselov, A. K. Geim, S. V. Morozov, D. Jiang, Y. Zhang, S. V. Dubonos, I. V. Grigorieva, and A. A. Firsov, Electric field effect in atomically thin carbon films, Science **306**, 666 (2004).

[4] B. Radisavljevic, A. Radenovic, J. Brivio, V. Giacometti, and A. Kis, Single-layer MoS_2 transistors, Nat. Nanotechnol. **6**, 147 (2011).

[5] S. Datta and B. Das, Electronic analog of the electro-optic modulator, Appl. Phys. Lett. **56**, 665 (1990).

[6] W. Han, Perspectives for spintronics in 2D materials, APL Mater. **4**, 032401 (2016).

[7] I. Choudhuri, P. Bhauriyal, and B. Pathak, Recent advances in graphene-like 2D materials for spintronics applications, Chem. Mater. **31**, 8260 (2019).

[8] Y. Liu, Y. Gao, S. Zhang, J. He, J. Yu, and Z. Liu, Valleytronics in transition metal dichalcogenides materials, Nano Res. **12**, 2695 (2019).

[9] J. R. Schaibley, H. Yu, G. Clark, P. Rivera, J. S. Ross, K. L. Seyler, W. Yao, and X. Xu, Valleytronics in 2D materials, Nat. Rev. Mater. **1**, 16055 (2016).

[10] D. Xiao, G.-B. Liu, W. Feng, X. Xu, and W. Yao, Coupled Spin and Valley Physics in Monolayers of MoS_2 and Other Group-VI Dichalcogenides, Phys. Rev. Lett. **108**, 196802 (2012).

[11] W. Yao, D. Xiao, and Q. Niu, Valley-dependent optoelectronics from inversion symmetry breaking, Phys. Rev. B **77**, 235406 (2008).

[12] A. Manchon, H. C. Koo, J. Nitta, S. M. Frolov, and R. A. Duine, New perspectives for Rashba spin-orbit coupling, Nat. Mater. **14**, 871 (2015).

[13] J. D. Koralek, C. P. Weber, J. Orenstein, B. A. Bernevig, S.-C. Zhang, S. Mack, and D. D. Awschalom, Emergence of the persistent spin helix in semiconductor quantum wells, Nature (London) **458**, 610 (2009).

[14] A. Sasaki, S. Nonaka, Y. Kunihashi, M. Kohda, T. Bauernfeind, T. Dollinger, K. Richter, and J. Nitta, Direct determination of spin-orbit interaction coefficients and realization of the persistent spin helix symmetry, Nat. Nanotechnol. **9**, 703 (2014).

[15] L. Zhu, Y. Zhang, P. Lin, Y. Wang, L. Yang, L. Chen, L. Wang, B. Chen, and Z. L. Wang, Piezotronic effect on Rashba spin-orbit coupling in a ZnO/P3HT nanowire array structure, ACS Nano **12**, 1811 (2018).

[16] S. Datta, How we proposed the spin transistor, Nat. Electron. **1**, 604 (2018).

[17] M. K. Mohanta, F. IS, A. Kishore, and A. De Sarkar, Spin-current modulation in hexagonal buckled ZnTe and CdTe monolayers for self-powered flexible-piezo-spintronic devices, ACS Appl. Mater. Interfaces **13**, 40872 (2021).

[18] F. IS, M. K. Mohanta, and A. D. Sarkar, Insights into selected 2D piezo Rashba semiconductors for self-powered flexible piezo spintronics: Material to contact properties, J. Phys.: Condens. Matter **35**, 253001 (2023).

[19] M. K. Mohanta, A. Arora, and A. De Sarkar, Conflux of tunable Rashba effect and piezoelectricity in flexible magnesium monochalcogenide monolayers for next-generation spintronic devices, Nanoscale **13**, 8210 (2021).

[20] M. D'yakonov, Spin relaxation of two-dimensional electrons in non-centrosymmetric semiconductors, Sov. Phys. Semicond. **20**, 110 (1986).

[21] J. Schliemann, Colloquium: Persistent spin textures in semiconductor nanostructures, Rev. Mod. Phys. **89**, 011001 (2017).

[22] J. Schliemann, J. C. Egues, and D. Loss, Nonballistic Spin-Field-Effect Transistor, Phys. Rev. Lett. **90**, 146801 (2003).

[23] M. P. Walser, C. Reichl, W. Wegscheider, and G. Salis, Direct mapping of the formation of a persistent spin helix, Nat. Phys. **8**, 757 (2012).

[24] M. Kohda, V. Lechner, Y. Kunihashi, T. Dollinger, P. Olbrich, C. Schönhuber, I. Caspers, V. V. Bel'kov, L. E. Golub, D. Weiss *et al.*, Gate-controlled persistent spin helix state in (In,Ga)As quantum wells, Phys. Rev. B **86**, 081306 (2012).

[25] F. Dettwiler, J. Fu, S. Mack, P. J. Weigele, J. C. Egues, D. D. Awschalom, and D. M. Zumbühl, Stretchable Persistent Spin Helices in GaAs Quantum Wells, Phys. Rev. X **7**, 031010 (2017).

[26] B. A. Bernevig, J. Orenstein, and S.-C. Zhang, Exact SU(2) Symmetry and Persistent Spin Helix in a Spin-Orbit Coupled System, Phys. Rev. Lett. **97**, 236601 (2006).

[27] L. L. Tao and E. Y. Tsymbal, Persistent spin texture enforced by symmetry, Nat. Commun. **9**, 2763 (2018).

[28] C. Autieri, P. Barone, J. Sławińska, and S. Picozzi, Persistent spin helix in Rashba-Dresselhaus ferroelectric $CsBiNb_2O_7$, Phys. Rev. Mater. **3**, 084416 (2019).

[29] H. Ai, X. Ma, X. Shao, W. Li, and M. Zhao, Reversible out-of-plane spin texture in a two-dimensional ferroelectric material for persistent spin helix, Phys. Rev. Mater. **3**, 054407 (2019).

[30] M. A. U. Absor and F. Ishii, Doping-induced persistent spin helix with a large spin splitting in monolayer SnSe, Phys. Rev. B **99**, 075136 (2019).

[31] M. A. U. Absor and F. Ishii, Intrinsic persistent spin helix state in two-dimensional group-IV monochalcogenide MX monolayers (M = Sn or Ge and X = S, Se, or Te), Phys. Rev. B **100**, 115104 (2019).

[32] H. Lee, J. Im, and H. Jin, Emergence of the giant out-of-plane Rashba effect and tunable nanoscale persistent spin helix in ferroelectric SnTe thin films, Appl. Phys. Lett. **116**, 022411 (2020).

[33] C. Bradley and A. Cracknell, *The Mathematical Theory of Symmetry in Solids: Representation Theory for Point Groups and Space Groups* (Oxford University Press, Oxford, 2010).

[34] See Supplemental Material at http://link.aps.org/supplemental/10.1103/PhysRevB.108.085432 for schematic of two nonsymmorphic space group symmetries: (a) glide plane and (b) screw axis; geometrical view of the (110) plane in zinc-blende bulk CdTe structure; general positions of space group No. 31; detailed analysis of symmetry operations in nonsymmorphic space group No. 31, SU(2) group; and some properties of the time-reversal operator.

[35] Y. X. Zhao and A. P. Schnyder, Nonsymmorphic symmetry-required band crossings in topological semimetals, Phys. Rev. B **94**, 195109 (2016).

[36] L. Michel and J. Zak, Connectivity of energy bands in crystals, Phys. Rev. B **59**, 5998 (1999).

[37] S. M. Young and C. L. Kane, Dirac Semimetals in Two Dimensions, Phys. Rev. Lett. **115**, 126803 (2015).

[38] A. Furusaki, Weyl points and Dirac lines protected by multiple screw rotations, Sci. Bull. **62**, 788 (2017).

[39] B.-J. Yang, T. A. Bojesen, T. Morimoto, and A. Furusaki, Topological semimetals protected by off-centered symmetries in nonsymmorphic crystals, Phys. Rev. B **95**, 075135 (2017).

[40] H. Wu, A. M. Hallas, X. Cai, J. Huang, J. S. Oh, V. Loganathan, A. Weiland, G. T. McCandless, J. Y. Chan, S.-K. Mo *et al.*, Nonsymmorphic symmetry-protected band crossings in a square-net metal $PtPb_4$, npj Quantum Mater. **7**, 31 (2022).

[41] G. Dresselhaus, Spin-orbit coupling effects in zinc blende structures, Phys. Rev. **100**, 580 (1955).

[42] B. Jusserand, D. Richards, G. Allan, C. Priester, and B. Etienne, Spin orientation at semiconductor heterointerfaces, Phys. Rev. B **51**, 4707 (1995).

[43] S. D. Ganichev, V. V. Bel'kov, L. E. Golub, E. L. Ivchenko, P. Schneider, S. Giglberger, J. Eroms, J. De Boeck, G. Borghs, W. Wegscheider *et al.*, Experimental Separation of Rashba and Dresselhaus Spin Splittings in Semiconductor Quantum Wells, Phys. Rev. Lett. **92**, 256601 (2004).

[44] J. B. Miller, D. M. Zumbühl, C. M. Marcus, Y. B. Lyanda-Geller, D. Goldhaber-Gordon, K. Campman, and A. C. Gossard, Gate-Controlled Spin-Orbit Quantum Interference Effects in Lateral Transport, Phys. Rev. Lett. **90**, 076807 (2003).

[45] Y. A. Bychkov and É. I. Rashba, Properties of a 2D electron gas with lifted spectral degeneracy, JETP Lett. **39**, 78 (1984).

[46] J. Schliemann and D. Loss, Anisotropic transport in a two-dimensional electron gas in the presence of spin-orbit coupling, Phys. Rev. B **68**, 165311 (2003).

[47] M. Trushin and J. Schliemann, Spin dynamics in rolled-up two-dimensional electron gases, New J. Phys. **9**, 346 (2007).

[48] K.-H. Jin, E. Oh, R. Stania, F. Liu, and H. W. Yeom, Enhanced berry curvature dipole and persistent spin texture in the Bi(110) monolayer, Nano Lett. **21**, 9468 (2021).

[49] J. Sławińska, F. T. Cerasoli, P. Gopal, M. Costa, S. Curtarolo, and M. B. Nardelli, Ultrathin SnTe films as a route towards all-in-one spintronics devices, 2D Mater. **7**, 025026 (2020).

[50] A. Jain, S. P. Ong, G. Hautier, W. Chen, W. D. Richards, S. Dacek, S. Cholia, D. Gunter, D. Skinner, G. Ceder *et al.*, Commentary: The Materials Project: A materials genome approach to accelerating materials innovation, APL Mater. **1**, 011002 (2013).

[51] Z. S. Popović, J. M. Kurdestany, and S. Satpathy, Electronic structure and anisotropic Rashba spin-orbit coupling in monolayer black phosphorus, Phys. Rev. B **92**, 035135 (2015).

[52] L. C. Gomes and A. Carvalho, Phosphorene analogues: Isoelectronic two-dimensional group-IV monochalcogenides with orthorhombic structure, Phys. Rev. B **92**, 085406 (2015).

[53] J. Kim, K.-W. Kim, D. Shin, S.-H. Lee, J. Sinova, N. Park, and H. Jin, Prediction of ferroelectricity-driven berry curvature enabling charge- and spin-controllable photocurrent in tin telluride monolayers, Nat. Commun. **10**, 3965 (2019).

[54] C. Rinaldi, S. Varotto, M. Asa, J. Sławińska, J. Fujii, G. Vinai, S. Cecchi, D. Di Sante, R. Calarco, I. Vobornik *et al.*, Ferroelectric control of the spin texture in GeTe, Nano Lett. **18**, 2751 (2018).

[55] G. Bian, X. Wang, T. Miller, T.-C. Chiang, P. J. Kowalczyk, O. Mahapatra, and S. A. Brown, First-principles and spectroscopic studies of Bi(110) films: Thickness-dependent Dirac modes and property oscillations, Phys. Rev. B **90**, 195409 (2014).

[56] K.-H. Jin, H. Huang, Z. Wang, and F. Liu, A 2D nonsymmorphic Dirac semimetal in a chemically modified group-VA monolayer with a black phosphorene structure, Nanoscale **11**, 7256 (2019).

[57] M. Kim, J. Im, A. J. Freeman, J. Ihm, and H. Jin, Switchable $S = \frac{1}{2}$ and $J = \frac{1}{2}$ Rashba bands in ferroelectric halide perovskites, Proc. Natl. Acad. Sci. USA **111**, 6900 (2014).

[58] L. Zhang, C. Tang, C. Zhang, and A. Du, First-principles screening of novel ferroelectric MXene phases with a large piezoelectric response and unusual auxeticity, Nanoscale **12**, 21291 (2020).

[59] W. Ding, J. Zhu, Z. Wang, Y. Gao, D. Xiao, Y. Gu, Z. Zhang, and W. Zhu, Prediction of intrinsic two-dimensional ferroelectrics in In_2Se_3 and other III_2-VI_3 van der Waals materials, Nat. Commun. **8**, 14956 (2017).

[60] R. Fei, W. Kang, and L. Yang, Ferroelectricity and Phase Transitions in Monolayer Group-IV Monochalcogenides, Phys. Rev. Lett. **117**, 097601 (2016).

[61] S. Singh and A. H. Romero, Giant tunable Rashba spin splitting in a two-dimensional BiSb monolayer and in BiSb/AlN heterostructures, Phys. Rev. B **95**, 165444 (2017).

[62] S. Sheoran, S. Monga, A. Phutela, and S. Bhattacharya, Coupled spin-valley, Rashba effect, and hidden spin polarization in WSi_2N_4 family, J. Phys. Chem. Lett. **14**, 1494 (2023).

[63] K. Wu, J. Chen, H. Ma, L. Wan, W. Hu, and J. Yang, Two-dimensional giant tunable Rashba semiconductors with two-atom-thick buckled honeycomb structure, Nano Lett. **21**, 740 (2021).

[64] Q.-F. Yao, J. Cai, W.-Y. Tong, S.-J. Gong, J.-Q. Wang, X. Wan, C.-G. Duan, and J. H. Chu, Manipulation of the large Rashba spin splitting in polar two-dimensional transition-metal dichalcogenides, Phys. Rev. B **95**, 165401 (2017).

[65] L. Xiang, Y. Ke, and Q. Zhang, Tunable giant Rashba-type spin splitting in $PtSe_2/MoSe_2$ heterostructure, Appl. Phys. Lett. **115**, 203501 (2019).

[66] Y. Ma, Y. Dai, W. Wei, X. Li, and B. Huang, Emergence of electric polarity in BiTeX (X = Br and I) monolayers and the giant Rashba spin splitting, Phys. Chem. Chem. Phys. **16**, 17603 (2014).

[67] A. Splendiani, L. Sun, Y. Zhang, T. Li, J. Kim, C.-Y. Chim, G. Galli, and F. Wang, Emerging photoluminescence in monolayer MoS_2, Nano Lett. **10**, 1271 (2010).

[68] J. Park, M. S. Kim, E. Cha, J. Kim, and W. Choi, Synthesis of uniform single layer WS_2 for tunable photoluminescence, Sci. Rep. **7**, 16121 (2017).

[69] J. Britt and C. Ferekides, Thin-film CdS/CdTe solar cell with 15.8% efficiency, Appl. Phys. Lett. **62**, 2851 (1993).

[70] T. Aramoto, S. Kumazawa, H. Higuchi, T. Arita, S. Shibutani, T. Nishio, J. Nakajima, M. Tsuji, A. Hanafusa, T. Hibino *et al.*, 16.0% Efficient thin-film CdS/CdTe solar cells, Jpn. J. Appl. Phys. **36**, 6304 (1997).

[71] A. Bosio, G. Rosa, and N. Romeo, Past, present and future of the thin film CdTe/CdS solar cells, Sol. Energy **175**, 31 (2018).

[72] R. G. Chaudhuri, A. Chaturvedi, and E. Iype, Visible light active 2D C_3N_4−CdS hetero-junction photocatalyst for effective removal of azo dye by photodegradation, Mater. Res. Express **5**, 036202 (2018).

[73] Q.-Q. Bi, J.-W. Wang, J.-X. Lv, J. Wang, W. Zhang, and T.-B. Lu, Selective photocatalytic CO_2 reduction in water by electrostatic assembly of CdS nanocrystals with a dinuclear cobalt catalyst, ACS Catal. **8**, 11815 (2018).

[74] P. Garg, S. Kumar, I. Choudhuri, A. Mahata, and B. Pathak, Hexagonal planar CdS monolayer sheet for visible light photocatalysis, J. Phys. Chem. C **120**, 7052 (2016).

[75] I. Repins, M. A. Contreras, B. Egaas, C. DeHart, J. Scharf, C. L. Perkins, B. To, and R. Noufi, 19·9%-efficient ZnO/CdS/$CuInGaSe_2$ solar cell with 81·2% fill factor, Prog. Photovolt. Res. Appl. **16**, 235 (2008).

[76] M. A. U. Absor, A. Lukmantoro, and I. Santoso, Full-zone persistent spin textures with giant spin splitting in two-dimensional group IV–V compounds, J. Phys.: Condens. Matter **34**, 445501 (2022).

[77] N. Higashitarumizu, H. Kawamoto, C.-J. Lee, B.-H. Lin, F.-H. Chu, I. Yonemori, T. Nishimura, K. Wakabayashi, W.-H. Chang, and K. Nagashio, Purely in-plane ferroelectricity in monolayer SnS at room temperature, Nat. Commun. **11**, 2428 (2020).

[78] X. Cartoixà, D. Z.-Y. Ting, and Y.-C. Chang, A resonant spin lifetime transistor, Appl. Phys. Lett. **83**, 1462 (2003).

[79] M. Khazaei, A. Ranjbar, M. Ghorbani-Asl, M. Arai, T. Sasaki, Y. Liang, and S. Yunoki, Nearly free electron states in MXenes, Phys. Rev. B **93**, 205125 (2016).

[80] M. K. Mohanta, I. S. Fathima, and A. De Sarkar, Exceptional mechano-electronic properties in the HfN_2 monolayer: A promising candidate in low-power flexible electronics, memory devices and photocatalysis, Phys. Chem. Chem. Phys. **22**, 21275 (2020).

[81] M. A. U. Absor, Y. Faishal, M. Anshory, I. Santoso, H. Sholihun, and F. Ishii, Highly persistent spin textures with giant tunable spin splitting in the two-dimensional germanium monochalcogenides, J. Phys.: Condens. Matter **33**, 305501 (2021).

[82] J. E. Hirsch, Spin Hall Effect, Phys. Rev. Lett. **83**, 1834 (1999).

[83] J. Wunderlich, B.-G. Park, A. C. Irvine, L. P. Zârbo, E. Rozkotová, P. Nemec, V. Novák, J. Sinova, and T. Jungwirth, Spin Hall effect transistor, Science **330**, 1801 (2010).

[84] J. Wunderlich, A. C. Irvine, J. Sinova, B. G. Park, L. P. Zârbo, X. L. Xu, B. Kaestner, V. Novák, and T. Jungwirth, Spin-injection Hall effect in a planar photovoltaic cell, Nat. Phys. **5**, 675 (2009).

[85] O. Çakıroğlu, J. O. Island, Y. Xie, R. Frisenda, and A. Castellanos-Gomez, An automated system for strain engineering and straintronics of 2D materials, Adv. Mater. Technol. **8**, 2201091 (2023).

[86] Y. Han, J. Zhou, H. Wang, L. Gao, S. Feng, K. Cao, Z. Xu, and Y. Lu, Experimental nanomechanics of 2D materials for strain engineering, Appl. Nanosci. **11**, 1075 (2021).

[87] Z. Peng, X. Chen, Y. Fan, D. J. Srolovitz, and D. Lei, Strain engineering of 2D semiconductors and graphene: From strain fields to band-structure tuning and photonic applications, Light Sci. Appl. **9**, 190 (2020).

[88] Y. Wang, C. Cong, W. Yang, J. Shang, N. Peimyoo, Y. Chen, J. Kang, J. Wang, W. Huang, and T. Yu, Strain-induced direct-indirect bandgap transition and phonon modulation in monolayer WS_2, Nano Res. **8**, 2562 (2015).

[89] M. Dienwiebel, G. S. Verhoeven, N. Pradeep, J. W. M. Frenken, J. A. Heimberg, and H. W. Zandbergen, Superlubricity of Graphite, Phys. Rev. Lett. **92**, 126101 (2004).

[90] M. Yankowitz, K. Watanabe, T. Taniguchi, P. San-Jose, and B. J. LeRoy, Pressure-induced commensurate stacking of graphene on boron nitride, Nat. Commun. **7**, 13168 (2016).

[91] S. M. Clark, K.-J. Jeon, J.-Y. Chen, and C.-S. Yoo, Few-layer graphene under high pressure: Raman and x-ray diffraction studies, Solid State Commun. **154**, 15 (2013).

[92] S. Yang, Y. Chen, and C. Jiang, Strain engineering of two-dimensional materials: Methods, properties, and applications, InfoMat **3**, 397 (2021).

[93] M. K. Mohanta and A. De Sarkar, Coupled spin and valley polarization in monolayer HfN_2 and valley-contrasting physics at the HfN_2-WSe_2 interface, Phys. Rev. B **102**, 125414 (2020).

[94] Y. Sun, Z. Sun, S. Gao, H. Cheng, Q. Liu, J. Piao, T. Yao, C. Wu, S. Hu, S. Wei *et al.*, Fabrication of flexible and freestanding zinc chalcogenide single layers, Nat. Commun. **3**, 1057 (2012).

[95] E. A. Soares, V. E. de Carvalho, and V. B. Nascimento, A layer-by-layer study of CdTe(110) surface Debye temperature and thermal vibrations by low energy electron diffraction, Surf. Sci. **431**, 74 (1999).

[96] K. Watari, J. L. A. Alves, and A. C. Ferraz, Atomic structures of CdTe and CdSe (110) surfaces, Braz. J. Phys. **26**, 271 (1996).

[97] G. Kresse and J. Furthmüller, Efficient iterative schemes for *ab initio* total-energy calculations using a plane-wave basis set, Phys. Rev. B **54**, 11169 (1996).

[98] G. Kresse and J. Furthmüller, Efficiency of *ab-initio* total energy calculations for metals and semiconductors using a plane-wave basis set, Comput. Mater. Sci. **6**, 15 (1996).

[99] J. P. Perdew, K. Burke, and M. Ernzerhof, Generalized Gradient Approximation Made Simple, Phys. Rev. Lett. **77**, 3865 (1996).

[100] P. E. Blöchl, Projector augmented-wave method, Phys. Rev. B **50**, 17953 (1994).

[101] A. Togo and I. Tanaka, First principles phonon calculations in materials science, Scr. Mater. **108**, 1 (2015).

[102] U. Herath, P. Tavadze, X. He, E. Bousquet, S. Singh, F. Muñoz, and A. H. Romero, PyProcar: A python library for electronic structure pre/post-processing, Comput. Phys. Commun. **251**, 107080 (2020).

[103] R. Resta, Theory of the electric polarization in crystals, Ferroelectrics **136**, 51 (1992).

[104] R. Resta, Macroscopic polarization in crystalline dielectrics: The geometric phase approach, Rev. Mod. Phys. **66**, 899 (1994).

[105] R. D. King-Smith and D. Vanderbilt, Theory of polarization of crystalline solids, Phys. Rev. B **47**, 1651 (1993).

[106] J. Qiao, J. Zhou, Z. Yuan, and W. Zhao, Calculation of intrinsic spin Hall conductivity by Wannier interpolation, Phys. Rev. B **98**, 214402 (2018).

[107] A. A. Mostofi, J. R. Yates, Y.-S. Lee, I. Souza, D. Vanderbilt, and N. Marzari, WANNIER90: A tool for obtaining maximally-localised Wannier functions, Comput. Phys. Commun. **178**, 685 (2008).

[108] G. Pizzi, V. Vitale, R. Arita, S. Blügel, F. Freimuth, G. Géranton, M. Gibertini, D. Gresch, C. Johnson, T. Koretsune *et al.*, WANNIER90 as a community code: New features and applications, J. Phys.: Condens. Matter **32**, 165902 (2020).

[109] A. Damle, L. Lin, and L. Ying, SCDM-k: Localized orbitals for solids via selected columns of the density matrix, J. Comput. Phys. **334**, 1 (2017).

[110] P. Giannozzi, O. Andreussi, T. Brumme, O. Bunau, M. B. Nardelli, M. Calandra, R. Car, C. Cavazzoni, D. Ceresoli, M. Cococcioni *et al.*, Advanced capabilities for materials modelling with QUANTUM ESPRESSO, J. Phys.: Condens. Matter **29**, 465901 (2017).

[111] P. Giannozzi, S. Baroni, N. Bonini, M. Calandra, R. Car, C. Cavazzoni, D. Ceresoli, G. L. Chiarotti, M. Cococcioni, I. Dabo *et al.*, QUANTUM ESPRESSO: A modular and open-source software project for quantum simulations of materials, J. Phys.: Condens. Matter **21**, 395502 (2009).

[112] G. Y. Guo, S. Murakami, T.-W. Chen, and N. Nagaosa, Intrinsic Spin Hall Effect in Platinum: First-Principles Calculations, Phys. Rev. Lett. **100**, 096401 (2008).